

Cis-clustering of cadherin-23 controls the kinetics of cell-cell adhesion

Sabyasachi Rakshit (✉ srakshit@iisermohali.ac.in)

Indian Institute of Science Education and Research Mohali <https://orcid.org/0000-0002-8083-6857>

Cheemeni Srinivas

Indian Institute of Science Education and Research Mohali

Gayathri Singaraju

Indian Institute of Science Education and Research Mohali

Nisha Arora

Indian Institute of Science Education and Research Mohali

Sayan Das

The Pennsylvania State University

Amin Sagar

Institute of Microbial Technology <https://orcid.org/0000-0002-6207-9557>

Anuj Kumar

Indian Institute of Science Education and Research Mohali

Article

Keywords: cadherin-23, cis-clustering, cell-cell adhesion

Posted Date: June 22nd, 2021

DOI: <https://doi.org/10.21203/rs.3.rs-622959/v1>

License:  This work is licensed under a Creative Commons Attribution 4.0 International License.

[Read Full License](#)

Cis-clustering of cadherin-23 controls the kinetics of cell-cell adhesion

Cheerani Sai Srinivas^{1#}, Gayathri Sindhuri Singaraju^{1#}, Nisha Arora¹, Sayan Das¹, Amin Sagar¹, Anuj Kumar², and Sabyasachi Rakshit^{1,3*}

¹Department of Chemical Sciences, Indian Institute of Science Education and Research Mohali, Punjab, India.

²Department of Physical Sciences, Indian Institute of Science Education and Research Mohali, Punjab, India.

³Centre for Protein Science Design and Engineering, Indian Institute of Science Education and Research Mohali, Punjab, India.

*Correspondence to Sabyasachi Rakshit

Email: srakshit@iisermohali.ac.in

Equal contributions

Abstract

Cis and trans-interactions in cadherins are the foundations of cellular adhesions in multicellular organisms. While the trans-interactions mediate the intercellular attachment, the cis-interaction is presumed as reinforcement to trans. Thus, trans precedes cis has been the well-accepted model in cadherin adhesion. The stronger affinity of trans-binding over cis has been the decisive influence in the trans first model. Here we show that cadherin-23, a non-classical cadherin with an extended extracellular region, can undergo cis-clustering in solution independent of trans and phase separate as liquid droplets. Using single-molecule measurements, we decipher that weaker cis-interactions favor the cis-clustering. *In-cellulo*, the cis-clustering is manifested as puncta, a common feature in non-classical cadherin junctions, and accelerates the cell adhesion. The cis-clustering thus kinetically controls cell-adhesion before trans-binding. Notably, M2-macrophages predominantly express cadherin-23 and rapidly attach to circulatory tumor cells during metastatic migration. However, the relation of cis-clustering with rapid cell-cell adhesion in physiology is not yet established.

Introduction

Cadherins predominantly maneuver the active cell-adhesion processes for both vertebrates and invertebrates. Two modes of binding are known for cadherins, trans-binding, and cis-binding. While in trans-binding, the terminal extracellular (EC) domains of cadherins from opponent cells interact with each other, the cis-binding is mediated by the lateral interactions among the rest of the EC domains of cadherins from the same cell surfaces(Harrison et al., 2011). Interestingly, no

direct experiment is performed to manifest the functional feature of cis-binding independent of trans-interactions. Cis-interaction is thus conceptually referred to as reinforcement to the trans-mediated cellular junctions. While trans mediates direct contacts among opposing cells and secures a junction, cis influences the clustering of cadherins at the junctions. Lack of direct experimental evidence thus presumably considers the clustering via cis as a foundation of trans-bonds. However, this need not be universally true.

The large conformational entropy and homotypic protein-protein repulsions against weak cis-interactions have been the limitations for cis clusters in solution. Results from molecular dynamics and Monte-Carlo simulations conceptualized the two-dimensional confinement of proteins as a solution to reduce the conformational entropy and neutralization of protein-protein repulsions, favoring independent cis clusters for classical cadherins. The strength of the cis-interaction is experimentally verified with E-cadherins on a supported lipid bilayer and monitored using single-particle tracking and FRET(Thompson et al., 2019, Thompson et al., 2020). However, capturing cadherin clusters mediated predominantly by cis-interactions in traditional solution-phase assays and studying their functional relevance has still been elusive yet demanding.

Clustering of solute in a solution is a classical phase separation to condensed phase from the dilute phase. In cell biology, such a liquid-liquid phase separation (LLPS) is common in the cytoplasm. It is the developmental origin of the membrane-less liquid compartments like nucleoli(Latonen, 2019), centrosomes(Mahen and Venkitaraman, 2012), Cajal bodies(Gall, 2003), stress granules(Buchan and Parker, 2009). Relatively uncommon, but the existence of LLPS is also reported with proteins like Zonula Occludens (Beutel et al., 2019), nephrin(Banjade and Rosen, 2014) that are anchored to cell-membrane and mediate multiprotein cell-adhesion, signal transduction. Favorable interactions among like-neighbors are thermodynamically responsible for such phase separations. Such favorable interactions are also present in cadherins and drive cis-clustering on two-dimensional confinement; however, the conformational entropy and protein-protein repulsion often overpower the cis-clustering in solution. Intuitively, controlled tuning of the counterbalancing interactions may favour the clustering and, subsequently, the LLPS with cadherins.

We performed an unbiased *in silico* search using the catGRANULE algorithm(Mitchell et al., 2013, Klus et al., 2014) across the cadherin-superfamily of proteins and identified cadherin-23 (Cdh23) (NP_075859) protein with a high propensity to undergo LLPS. Cdh23 is one of the long non-classical classes of cadherins with 27 extracellular domains. It mediates strong cell-cell adhesion among tissues like the heart, kidney, muscle, and testis through homophilic interactions (Sannigrahi et al., 2019, Singaraju et al., 2019, Sotomayor et al., 2012), and heterophilic interactions with protocadherin-15 in neuroepithelial cells(Sotomayor et al., 2010). Interestingly, with the potential for multivalent lateral interactions, Cdh23 engages in a stable spiral cis-dimerization(Kachar et al., 2000). Here using single-molecule force spectroscopy, we estimated the cis-interactions of Cdh23 quantitatively and verified their multivalency. Notably, this is the first-ever quantitative measure of cis-interactions of any cadherin protein. The cis-interactions of Cdh23 facilitate clustering and phase separate to liquid droplets in solution. The phenomenon is

critical to the ionic strength of the buffer. We quantitatively derived the relation of cis-clustering with the elasticity and resilience of cis-complexes at varying ionic strength of buffers.

Interestingly, the strength and the elasticity (in terms of persistence length) of the cis-complex regulate the phase separation of Cdh23 anti-correlatively. The in-cellulo manifestation of cis-clustering is featured as puncta in HEK293 cells exogenously expressing Cdh23. The functional consequence of such clustering is accelerated cell-cell adhesion of many-fold. Notably, while the toxicity of the phase-separated states has already been proposed for intrinsically disordered proteins(Elbaum-Garfinkle, 2019), the fast-aggregation of cells is a demonstration of the functional implication of LLPS in cell adhesion.

Results

Cdh23 with 27 EC domains undergoes LLPS

Extended EC domains may enhance the lateral interactions in Cdh23, and on the contrary, induce more conformational entropy in the system, eventually making the in-solution clustering again challenging. Interestingly, the presence of Ca^{2+} ions in the coordination sphere of cadherins reduces conformational variations. Further, inert polymers like polyethylene glycol (PEG) molecules often occupy the excluded protein volume and reduce protein entropy(Kaur et al., 2019, Delarue et al., 2018). Besides, Cdh23 EC1-27 has 440 negatively charged and 222 positively charged amino acid residues distributed throughout its structure, thus possessing coacervation propensity. It is, therefore, an interplay between the concentration of Ca^{2+} ions, ionic strength of the buffer, and the protein proximity that is to optimize the lateral interactions in Cdh23 and drive phase separation in solution. Our *in-silico* search identified the EC regions in Cdh23 as more prone towards phase separation with a propensity score of 1.3. Usually, a propensity score higher than 1 is considered a good LLPS candidate(Ambadipudi et al., 2017). However, the propensity score for Cdh23 EC1-10, a version of truncated isoform, was measured lower than 1 (Fig. S1). Inference from the crystallographic studies has also revealed EC domains 14, 17, 20, 21, 23, and 25 as predominantly responsible for cis-interactions in Cdh23(Jaiganesh et al., 2018). To verify, we designed two variants of Cdh23: Cdh23 EC1-27, a variant with an entire EC region, thus possessing high-propensity for LLPS, and a truncated version, Cdh23 EC1-10, with a low-propensity for LLPS. Subsequently, we performed single-molecule force-ramp spectroscopy (SMFS) to precisely quantify the strength of cis-interactions among respective variants using an atomic force microscope (AFM) (Fig.1 A). For SMFS, the C-termini of both the protein variants were recombinantly modified with sort-tag and ESCORTed to AFM cantilevers and glass-coverslips, respectively(Srinivasan et al., 2017). Reportedly, Cdh23, apart from cis-interactions, can mediate both homophilic and heterophilic trans-interactions. It was, therefore, necessary to block the interference of the trans-interactions to measure the strength of cis-binding. Notably, the heterophilic trans-interaction with Pcdh15 has the highest affinity in the list(Choudhary et al., 2020, Singaraju et al., 2019, Sotomayor et al., 2012). We, therefore, used excess Pcdh15 (5 μM Pcdh15 EC1-2) in the experiment buffer to neutralize the trans-binding interface of Cdh23 and predominantly measured the homophilic cis-

interactions (Materials and methods). The non-specificity in the measurements was judiciously quantified and filtered out (Materials and Methods). Finally, we obtained nearly 3% of specific events featuring sliding-unzipping. The sliding-unzipping features in the force-extension curves are typical for the unbinding of spatially distributed multiple interacting points, as expected in cis-dimers of Cdh23 (Fig. 1 A and B). Two weak unzippings with extensions of 22.8 ± 0.4 nm and 12.7 ± 0.8 nm, respectively, were noticed, followed by a final disruption of the complex (Fig. S2 and Fig. 3 A and B). If we average individual domain-length as 5 nm (based on crystal structure), the extensions after unzipping refer to two interacting points that are separated by 4 ($22/5 \sim 4$) EC domains and 2 ($12/5 \sim 2$) EC domains, respectively. The first unzipping was noticed after an entropic elongation of 60.1 ± 1.3 nm (Fig. S3 A). We next analyzed the most probable force (F_{mp}) of the final complex disruption at varying loading rates and obtained the kinetic parameters of the complex from the Bell-Evan's model fit (Fig. 1 C and D) (Materials and Methods). The intrinsic off-rate of the complex is 5.01 ± 0.02 s⁻¹, and the width of the potential barrier (x_β) is 0.24 ± 0.01 nm. As expected, the off-rate of cis-interactions is significantly higher than the previously measured off-rate for heterophilic ($4.5 \times 10^{-3} \pm 4.9 \times 10^{-5}$ s⁻¹) trans-interactions (Hazra et al., 2019), indicating that the homophilic cis-interactions is weaker in the race. Further, we performed SMFS to estimate the cis-interacting strength of Cdh23 EC1-10 following a similar protocol as Cdh23 EC1-27. As expected, we measured interactions comparable to non-specific measurements, indicating that the cis-binding affinity of Cdh23 EC1-10 is not detectable by SMFS using AFM.

To arrest the cis-clustering of Cdh23 EC1-27 in solution, we systematically varied the protein concentrations and the ionic strength of the buffer. We recombinantly tagged eGFP at the C-terminal of each variant to visually track the cis-induced phase separations in real-time under a fluorescence microscope. 20 mM of HEPES buffer at pH 7.5 was used for all experiments, and 0.5% of PEG6000 was used as a crowding agent. We noticed the condensates of Cdh23 EC1-27 proteins for a range of protein concentrations, ionic strengths, and Ca²⁺ concentrations (Fig. 1 E, F and G). Association of the green fluorescence with the protein confirmed that the condensates are made of Cdh23 (Fig. 1 F and Video 1 A). Fusion among floating droplets, the gold standard for liquid condensates, is too noticed among Cdh23 condensates, indicating the fluid nature of the droplets (Fig. 1 E and Video 1 B). Further from the time-trace analysis of the fusion events, we measured an average fusion-time of 5.0 ± 1.2 s, in range with other proteins that undergo LLPS (Wang et al., 2019) (Fig. S 4 and Video 1 B).

Attributing to the Hofmeister series, a standard theory to estimate protein stability and solubility, we systematically varied Na⁺ & Ca²⁺ ions to identify optimal conditions for the liquid-phase condensation of Cdh23 EC1-27 (Dignon et al., 2020). The rate of droplet growth was monitored for optimization (Fig. 1 G). Towards this, we first varied Na⁺ ions keeping Ca²⁺ ions fixed at 4 mM. We noticed a gradual increase in droplet growth rate with increasing Na⁺ ions, reaching an optimum at 500 mM (Fig. 1 G). The phase separation of Cdh23 EC1-27 was noticed for 100 mM – 1 M of NaCl. Next, we set the Na⁺ ions to 500 mM and altered Ca²⁺ ions and obtained phase

separation for a range of 4 mM – 10 mM of CaCl₂, and optimal at 6 mM of Ca²⁺(Fig. S5 A). Finally, we fixed the Ca²⁺ ions to 6 mM and varied both protein and Na⁺ ions to obtain a complete phase separation diagram (Fig. 1 H). The optimal growth rate of liquid droplets was obtained at 14 μM of proteins, 535 mM ionic strength, and 6 mM of Ca²⁺ ions (Fig. 1 G and H and Fig. S5 B and Fig. S6). We noted a lower critical concentration of 2.5 μM for Cdh23 EC1-27 for *in vitro* cis-clustering (Fig. 1 H). Also, Na⁺ and Ca²⁺ ions beyond the salting-out range showed no LLPS for Cdh23 EC1-27. It is important to note that the optimal Ca²⁺ ions for *in vitro* LLPS of Cdh23 EC1-27 are within the scope of the extracellular region in physiology.

We measured the cis-interactions of Cdh23 EC1-27 using SMFS at varying ionic strength and deciphered a relation of cis-interactions with the liquid droplets. The ionic strength of the buffer was varied by varying Na⁺ ions while keeping Ca²⁺ ions fixed at 4 mM, as previously. We noticed a gradual drop in the cis-interactions of Cdh23 EC1-27 with increasing ionic strength up to 400 mM of NaCl and, beyond that, a gradual increase. Interestingly, though the change in interaction strength with ionic strength follows a converse trend to the phase separation in solution, both undergo a critical transition at 400-500 mM NaCl. The change in the persistence length of the cis-complex as a measure of molecular elasticity follows a similar trend with the condensation of Cdh23 EC1-27 in solution (Fig. 1 I and Fig. S7). Overall, the data indicate a correlation of molecular elasticity with LLPS and a converse relation with the strength of the cis-interactions that drive the phase separation. We hypothesize that the changes in the protein conformation and the intrinsic and electrostatic persistence length of the protein with ionic strength of the buffer solution are critical for such a relation. We noticed an offset in the NaCl concentration for optimal soft condensation of Cdh23 EC1-27 (500 mM) and weakest cis-interactions (400 mM). The offset could be an artifact arising from the differences in the solution-based estimate of LLPS to the surface-based assessment in SMFS.

Interestingly, Cdh23 EC1-10 did not undergo phase separation for a wide range of buffer conditions, including the requirements maintained for Cdh23 EC1-27. We, therefore, considered the truncated version as the negative control. The point to note here is that both Cdh23 EC1-10 and Cdh23 EC1-27 have eGFP tags at their C-termini, and yet, Cdh23 EC1-27 is the only construct undergoing LLPS thus, withholding the significance of eGFP in LLPS.

To validate the LLPS of Cdh23 EC1-27 as a resultant of exclusive cis-clustering, we repeated the phase transition experiment in the optimal condition, but by blocking the trans-interacting sites with ligand-protein, Pcdh15 EC1-2. As a precaution, we facilitated the heterophilic trans-interactions first with an abundance of Pcdh15 EC1-2 in the experiment buffer and carefully altering the solution's ionic strength from an unfavorable phase separation condition to a favorable condition via dialysis (Materials and Methods). We observed LLPS of Cdh23 EC1-27 and Pcdh15 EC1-2 complex, indicating that the droplets are predominantly from cis-clustering of Cdh23(Fig. S8). Notably, the droplets of Cdh23 EC1-27 without Pcdh15 EC1-2 were more extensive than in the presence of Pcdh15 EC1-2, indicating that the trans-interactions enhance the phase separation but not essential for the LLPS. Overall, Cdh23 EC1-27 undergoes LLPS

under physiological conditions, and the liquid droplets follow the characteristic feature of protein condensates.

LLPS helps in faster cell-cell aggregation

Liquid droplets of Cdh23 are not exclusive to *in-vitro* conditions. We observed mesoscopic liquid-like assemblies of Cdh23 *in-cellulo* in HEK293 cells stably expressing full-length Cdh23. Full-length Cdh23, similar to the other cadherin family members, comprises a transmembrane domain and a cytosolic domain along with EC regions. Punctate structures in the mesoscopic to the microscopic regime were noticed at the cell-cell junctions of stably transfected HEK293 cells (Materials and Methods). The puncta structures were absent in control for immunofluorescence images, where only a secondary antibody was used for staining the cells (Fig. 2 A). Cellular droplets in cytosol separate homogeneous solution of biomolecules into two phases, a condensed liquid droplet of specific biomolecules surrounded by a diluted phase. Since the foundation of the condensed phase is transient and weak intermolecular interactions, the liquid phase rapidly and reversibly undergoes de-mixing in response to chemical and physical cues, either triggered by *in-cellulo* activities or externally. We performed the de-mixing of cellular droplets as confirmation for the fluidic nature of the puncta. 1,6-hexanediol is a widely used aliphatic alcohol in cell biology that weakens the hydrophobic interactions critical for LLPS and inhibits liquid droplets (Itoh et al., 2021, Duster et al., 2021). Accordingly, we treated the stable HEK293 cells with 1,6-hexanediol and monitored the disruption of puncta structures, confirming the fluid nature of the Cdh23 clusters in cells (Fig. 2 A).

How do the liquid droplets of Cdh23 mediated by cis-clustering contribute to cells? Cadherins generally form anchoring junctions with the neighboring cells. Cdh23 is no different from the other family members and mediates vital cell-cell adhesion junctions in several tissues like the kidney, muscle, testes, and heart (Singaraju et al., 2019, Sannigrahi et al., 2019, Sotomayor et al., 2012, Li et al., 2019). We, therefore, verified the effect of the liquid condensates of Cdh23 mediated by cis-clustering in cell-cell adhesion, more importantly where cis-clustering precedes the trans-interactions. We hypothesized that cis-clustering on a membrane would increase the effective intercellular interacting interface and accelerate cell-adhesion kinetics. We thus monitored the aggregation-kinetics of HEK293 cells exogenously expressing Cdh23. We fit the kinetics data to Von Bertalanffy model (West and Newton, 2019, Benzekry et al., 2014) to estimate the relative adhesion-rate constants (Materials and Methods). We used the same two recombinant variants, Cdh23 EC1-27 and Cdh23 EC1-10, but along with the transmembrane (TM) and cytosolic domains (CD) at their C-terminals (NP_075859). For monitoring the localization of proteins on cell junctions, we fused eGFP at the extreme C-terminals of the constructs. We transfected these chimeric constructs in HEK293 cells, where the cells were pre-treated with siRNA to silence the endogenous Cdh23 expression precisely (Materials and Methods). As expected, we observed a significant enhancement in the aggregation-kinetics of cells expressing Cdh23 EC1-27 (rate constant, $a_{on}^0 = 2.1 \times 10^{-3} \text{ min}^{-1}$) (Fig. 2 B) than the cells over-expressing Cdh23 EC1-10 ($a_{on}^0 = 3.4 \times 10^{-4} \text{ min}^{-1}$) (Fig. 2 C). Important to note that

both types of cells formed Cdh23-mediated matured cell-cell junction after incubation, warranting the functional activity of both constructs. HEK293 cells treated with siRNA for endogenous Cdh23 showed no aggregation within the experiment time.

To verify the relevance of the optimization conditions of LLPS of proteins in cellular aggregations, we developed the phase diagram of cell aggregations at varying Ca^{2+} ions. The LLPS of Cdh23 EC1-27 in solution is optimum at physiological Ca^{2+} content in the extracellular matrix. HEK293 cells overexpressing Cdh23 EC1-27 showed slower cell-aggregation propensity at low (0.5 mM Ca^{2+} ; $a_{on}^0 = 1.1 \times 10^{-3} \text{ min}^{-1}$) and very high (20 mM Ca^{2+} ; $a_{on}^0 = 1.3 \times 10^{-3} \text{ min}^{-1}$), and the optimum aggregation rate at 10 mM Ca^{2+} ($a_{on}^0 = 2.9 \times 10^{-3} \text{ min}^{-1}$), corroborating the optimal condition of LLPS of Cdh23 EC1-27 proteins *in vitro* (Fig. 2 D). It is important to note that despite low cell-aggregation rates, Cdh23 forms matured and strong cell-cell junction at as low as 0.5 mM Ca^{2+} (Fig. S9). Overall, the cell-aggregation data indicate that the cis-clustering of Cdh23 EC1-27 on a cell membrane kinetically accelerates the cell-to-cell anchorage. However, it eventually formed thermodynamically stable cell-cell junctions irrespective of cis-clustering mediated adhesions.

Does cis-clustering on cell-membrane depend on the endogenous expression of Cdh23? To check, we monitored the cell-aggregation kinetics among cancer cell-lines, HEK293, HeLa, HaCaT, and A549, that express endogenous Cdh23 differentially. Our results from qRT-PCR and western blot, in corroboration with TCGA, indicate higher endogenous expression of Cdh23 in A549, HaCaT cells and comparatively lower expression in HEK293, HeLa cell-lines (Fig. S10 A). Amongst all in the list, HeLa has the least expression. We performed the cell-aggregation assays in the previously optimized buffer condition and noticed significantly faster cell-aggregations in A549 and HaCat, than the low-expressing cell lines (HEK293 and HeLa). HeLa did not aggregate within the experiment time. Interestingly, all cell lines with relatively higher expression of Cdh23 showed comparable aggregation rates (Fig. 3 A and B), thus indicating that the clustering mediated aggregation probably requires a critical endogenous expression.

Discussion

Cdh23 can condensate to the punctate liquid phase at the cell membrane and, as super-adhesive, quickly seizes the floating cells into aggregates. Though dense, short-range punctate junctions are widely noted for the cadherin family of proteins, the physiological implication of rapid cell-cell adhesion/communication is still elusive. Here, we deciphered that the punctate could be liquid droplets of cadherins. In the family of cadherins, this is the first report to highlight the ability of the cadherin family of proteins to undergo LLPS. The LLPS mediated faster cell-cell adhesion is also the first demonstration of the physiological implication of LLPS on the membrane. Interestingly, Cdh23, among other cadherins, is significantly overexpressed in tumor-infiltrating M2-type macrophages (Poczobutt et al., 2016) and microglia (Zhang et al., 2016, Zhang et al., 2014) (Fig. S10 B). M2-type macrophages associate with the circulatory tumor cells (CTCs) on the go and help in metastasis. A quick cell-cell adhesion is thus essential in this process. Though speculative, the fast adhesion between M2 macrophages and CTCs is facilitated

by the condensed Cdh23 droplets. Further, Cdh23 in tip-links in neuroepithelial hair-cells partner with Pcdh15 and experience strong physical forces from sound-stimuli in hearing. Interestingly, the protein complexes (Myosin-7/Harmonin B) that anchor the cytosolic component of Cdh23 with the cytoskeleton of stereocilia in hair cells also form condensates via LLPS(He et al., 2019). Together, it is indicative that the condensate of Cdh23 on the cell membrane is physiologically relevant and needs to be explored.

Usually, multimodal interactions with modularity are among the driving forces for LLPS. The ectodomains of Cdh23 possess such multiple interaction sites, witnessed from the SMFS of cis-dimers and the puckered and extended coil conformation of Cdh23 cis-dimer(Jaiganesh et al., 2018, Di Palma et al., 2001). Interestingly, we noted that the weakest cis-dimer interactions are most favorable for LLPS. The propensity of LLPS of Cdh23 directly correlates with the persistence length of the cis-complex. The specific cis-interacting sites beyond the ectodomain number of 10 (dom10) were also identified from the fragmented crystal structures of Cdh23 domains(Jaiganesh et al., 2018). Further, the catGRANULE algorithm that predicts the LLPS propensity of a protein from the primary structure identified several granules forming sites on the ectodomains of Cdh23, majorly beyond dom10. Accordingly, we also observed LLPS for Cdh23 EC1-27 at the lowest concentration of 2.5 μM *in-vitro* but no condensed liquid-like phase for Cdh23 EC1-10 even at a very high concentration of 100 μM . Our *in-cellulo* experiments also featured multifold faster rate (a_{on}^0) of cellular aggregation for cell-lines expressing full-length Cdh23 (Cdh23 EC1-27+TM+CD) ($a_{on}^0 = 2.14 \times 10^{-3} \text{ min}^{-1}$) than the truncated form of Cdh23 (Cdh23 EC1-10+TM+CD) ($a_{on}^0 = 3.4 \times 10^{-4} \text{ min}^{-1}$). Together, our data indicate that the EC domains beyond 10 (EC10 – 27) are the key for LLPS.

Moreover, cadherin's cis-dimerization is generally considered the aftereffect of intercellular trans-interactions(Pontani et al., 2016). The physiological role of the cis-dimer is proposed to strengthen the trans-interactions at the cell-cell junction(Wu et al., 2010). The liquid phase condensate of Cdh23 on-membrane instead contributes to the kinetics of cell-cell adhesion. The spontaneous LLPS can affect the rate of cell-cell adhesion at the initial phase and may not affect the mature cell-cell junction. However, the physiological implication of such fast-snapping is still not well-understood.

Interestingly, Cdh23 may not be the only cadherin in the family that can undergo LLPS. The Catgranule algorithm estimated the CDF score of more than 1 for many other cadherins (Table 1), considering only the ectodomains. In general, with a CDF of more than 1, the proteins show a tendency for LLPS. Accordingly, Fat-cadherin, Dacshous-cadherin, desmosomes, cadherin-22 have CDF scores of more than 1 and can undergo LLPS. Interestingly, most of these cadherins are associated with special cell-cell junctions. For instance, fat-dachsous cadherin-mediated heterophilic junctions exclusively regulate the epithelial cell-size dynamics (ECD) under the mechanical cues during morphogenesis(Kumar et al., 2020), desmoglein-2 forms heterophilic interactions with other isoforms of desmosomal cadherins and form Ca^{2+} -independent hyper-adhesive desmosomal junctions in tissues like skin, heart that are exposed to physical forces. Apart from cadherins, ZO1 that form tight-junctions(McNeil et al., 2006) also has a CDF score of more than 1 and undergoes LLPS (Beutel et al., 2019).

Conclusion

The distinctive features of liquid droplets, stretchable and tunable to different sizes and shapes, may be helpful in cell-cell junction, which routinely experiences mechanical assault. Our results address a functional feature that liquid condensates can achieve, but the individual functional counterparts cannot. Identifying the physiological or pathological cues that trigger such phase transitions is the next exciting step and may open up another exciting field of rapid cell-cell communication and adhesion.

Materials and Methods

Cloning of domain deletion mutants of Cdh23

The full-length Cdh23(NP_075859) consisting of 27 EC domains, a transmembrane domain, and a cytoplasmic domain was a generous gift from Dr. Raj Ladher, NCBS, Bangalore. Using this construct, we recombinantly generated domain deletion mutants. We have subcloned the same construct in pcDNA3.1 (+) plasmid, which codes for Neomycin resistance. All the constructs were cloned between NheI and XhoI restriction sites with (S)-Sortase-tag (LPETGG)-(G)-eGFP-tag and (H)-His-tag; SGH-tag at downstream (C-terminus of the protein) in the same order. All the recombinant constructs were verified through double digestion, PCR amplification, and DNA sequencing.

Protein expression and purification

All recombinant Cdh23 variants for *in-vitro* studies were expressed in the ExpiCHO suspension cell system (A29129 ThermoFisher Scientific), following the prescribed protocol for transfection in ExpiCHO cells. After seven days, the culture media was collected by pelleting down the cells at 2000 rpm for 15 min at room temperature. The media was then extensively dialyzed against the dialysis buffer for 48 hours and intermittently changed the buffer every 8 hours. The dialyzed media with proteins were purified using affinity chromatography using Ni-NTA columns. The purity of the samples was checked using SDS-PAGE. Finally, the protein was confirmed using western blotting with specific antibodies against GFP, Cadherin-23, and his-tag.

Surface and cantilever tip modification

Glass-coverslips were activated using air plasma treatment, washed with freshly prepared piranha for 2 hours, and subsequently washed thoroughly with deionized water in bath sonicator three times, each for 10 min. Coverslips were then etched using 1M KOH for 15 min, followed by washing with deionized water by sonicating thrice for 10min each time. Cleaned surfaces and Si₃N₄ cantilevers (APPNANO NITRA-TALL) were silanized using 2% APTES (3-Aminopropyltriethoxy silane) (Sigma–Aldrich) in 95% acetone and cured at 110 °C for 1 hour. The amine exposed surfaces and cantilevers were functionalized with Maleimide-PEG2-Succinimidyl ester (Mal-PEG2-NHS) (Sigma–Aldrich) in a basic buffer (100 mM NaHCO₃, 600 mM K₂SO₄, pH 8.2) for 4 hours at room temperature. The PEGylated surfaces and cantilevers were then incubated with 100 μM polyglycine peptides, GGGGC for cysteine–maleimide reaction at room temperature for 7 hours, and then washed with water. Polyglycine on coverslips act as a nucleophile for sortagging.

Single-molecule force spectroscopy using AFM

C-terminus of Cdh23 was covalently attached to the polyglycine coated glass-coverslips and AFM cantilevers, using sortagging chemistry as described previously (Srinivasan et al., 2017). After protein attachment, we incubated the cantilever and surface with the excess of Pcdh15 EC1-2 to block the trans-homodimeric interactions (Sotomayor et al., 2012). We also maintained the Pcdh15 EC1-2 in the buffer solution during the experiment to exclusively facilitate cis-dimer formation.

After modifying the coverslip and cantilever with proteins, we performed dynamic force-ramp measurements using Atomic Force Microscope (AFM) (Nano wizard 3, JPK Instruments, Germany). During force-ramp, we brought the cantilever down at 2000 nm.s⁻¹, waited for 0.5 s for proteins to interact and form cis-dimer, and finally retracted the cantilever at velocities varying from 1000, 2000, 3000, 5000, and 7500 nm.s⁻¹. At each pulling speed, we recorded 6000 force curves. Analyses of the force-extension curves were performed using home-written MATLAB programs. All cantilevers were calibrated using the Thermal fluctuation method after modification and before use.

To estimate non-specificity in our SMFS, we performed control experiments by attaching the Cdh23 protein on the cantilever without any protein attachment on the polyglycine modified glass coverslip. We obtained 0.4% of events featuring an average total extension of 38.7±0.5 nm. The end-to-end extension in specific cis-dimer interactions is 94.4±1.4 nm (Fig. S11 A and B). We thus considered only those distinct force curves showing the cis-dimer feature and a total extension of more than 50 nm.

SMFS data Analysis and fitting to a model

Unbinding force (F) and change in the contour length during unzipping of cis-dimer was measured from the fitting of worm-like chain (WLC) equation of polymer elasticity (eqn 1) (Bustamante et al., 1994).

$$F(x) = \frac{k_B T}{l_p} \left[\frac{1}{4} \left(1 - \frac{x}{Lc} \right)^{-2} - \frac{1}{4} + \frac{x}{Lc} \right] \quad (1)$$

Where F is the unbinding force, l_p is the persistence length, x is the end-to-end length, and Lc is the contour length of the protein, k_B is the Boltzmann's constant, and T is the temperature.

Kinetic parameters like the intrinsic off-rate (k_{off}^0) and the distance to transition state (x_β) were obtained from the Bell-Evans model fitting of the most probable unbinding force (F) vs. loading rate (r) data (Bell, 1978, Evans and Ritchie, 1997),

$$F(r) = \left(\frac{k_B T}{x_\beta} \right) \ln \frac{r x_\beta}{k_{off}^0 k_B T} \quad (2)$$

In-vitro droplet-condensation assay

All purified proteins were prepared in buffer containing 20 mM HEPES, pH 7.5, 100 mM NaCl, 4 mM CaCl₂. Before each experiment, the proteins were centrifuged at 15000 rpm at 4°C for

10 min to remove possible non-specific aggregates. Then proteins were mixed or diluted to reach designated concentrations. Each protein mixture (14 μ M for each component) was injected into a homemade chamber and imaged using a Leica microscope (Leica DMI8) using 40X objective lens. The time-lapse images were taken under bright-field and fluorescence filters. All the assayed droplets were thicker than 6 μ m in height, so the central layers of optical sections were chosen for quantification. Over 10 or more droplets were measured for each protein to generate the phase diagram of the condensed phase. The images were analyzed by ImageJ, and the quantification was performed by Origin software.

Immunofluorescence and LLPS disruption studies

Immunofluorescence staining was performed using Cadherin-23 (HPA017232, Sigma-Aldrich) primary antibody and Anti Rabbit IGG CF633 (SAB4600141, Sigma-Aldrich) secondary antibody. DAPI (Sigma-Aldrich) was used to stain the nuclei of the cells. Images of immunofluorescent labeled cells were obtained on a confocal microscope (Leica, TCS SP8) using a 63X objective lens. To disrupt the liquid-like clusters, Cdh23 stable HEK293 cells were incubated with 2% (w/v) of 1,6-Hexanediol (H11807, Sigma-Aldrich) for 1 hour.

Cell line culture

The adherent cancer cell lines HeLa, HEK293, A549, and HaCat were obtained from NCCS, Pune. All cells were cultured in high glucose DMEM media (D1152, Sigma-Aldrich) containing 10% FBS and 5% CO₂. The suspension cell line, ExpiCHO (#A29127), was purchased from ThermoFisher Scientific and grown in ExpiCHO expression medium at 37 °C and 6% CO₂.

Western blot and qRT-PCR

We have followed the standard protocol(Hirano, 2012) for the western blotting of the cell lines. Cadherin-23 (HPA017232, Sigma-Aldrich and PA5-43398, Invitrogen), eGFP (A11122, Invitrogen) and His-tag (11965085001, Roche) antibodies were used to detect the proteins.

RNA from different cancer cell lines was extracted using RNA isolation kit (Bio-Rad) and treated with DNase using DNase 1 kit (AMPD1, Sigma-Aldrich). cDNA synthesis was done using cDNA synthesis kit (Bio-Rad). qRT-PCR was performed with the primers probing Cdh23 using the real-time PCR system (CFX96 Bio-Rad).

Cell-aggregation assay

After 30 hours of post-transfection, the cells were washed gently with PBS and then resuspended in Hank's buffer supplemented with 10 mM Ca²⁺ ions to a final cell count of 10⁵ cells. Hank's buffer behaves like an incomplete media maintaining the solution's osmolarity with the cells avoiding any bursting or shrinking of cells throughout the entire duration of the assay. After resuspending, the cells were imaged with a bright-field filter at 10X magnification using a Leica Inverted Microscope (Leica DMI8) over a time trace for 2 hours. The images were collected at 10 min, 15min, 30 min, 45 min, 60 min, and 120 min when all the cells aggregated completely. The image analysis for measuring the area of each aggregate was done in ImageJ software. The mean area of aggregates over four different focal positions was measured and plotted against time. The aggregate size was compared over varying domain lengths for Cdh23.

Fitting the cell aggregation data to a model

We have used Von Bertalanffy model (West and Newton, 2019, Benzekry et al., 2014) to quantify the rate of cell-cell aggregation for HEK293 cells transfected with Cdh23 EC1-10 and Cdh23 EC1-27 at different calcium concentrations. The net rate of cell aggregation is proportional to the total area of aggregate. In the absence of any dissociation in our experiment timescale, we have neglected the loss term in the equation (a special case of Von Bertalanffy model). Finally, we fit the cell aggregation data for an experimental condition over time using the following rate-equation:

$$\frac{dA}{dt} = a_{on}^0 \cdot A^\gamma$$

The model is solved and written explicitly

$$A(t) = (a_{on}^0 \cdot t \cdot (1 - \gamma))^{\frac{1}{1-\gamma}}$$

Where, a_{on}^0 represents the rate-constant, A represents the area of aggregate, t is the independent variable (time), and γ represents the growth of aggregate. a_{on}^0 is an inherent property, and γ is dependent on the cell types and their heterogeneity.

We performed all cell aggregation experiments at fixed cell types and numbers. While fitting, we, therefore, performed global fits and shared the value of γ (Table S1).

Acknowledgments

This work was supported by the DBT/Wellcome Trust India Alliance Fellowship [grant number: IA/I/15/1/501817] awarded to S.Rakshit.

S.Rakshit acknowledges and thanks to Dr. Raj K. Ladher, NCBS for generously donating the Cadherin-23 plasmid. S.Rakshit acknowledges the financial support by the DBT/Wellcome Trust India Alliance, Indian Institute of Science Education and Research Mohali (IISERM), and Centre for Protein Science Design and Engineering (CPSDE), Indian Institute of Science Education and Research Mohali. G.S.Singaraju, C.S.Srinivas and A.Sagar sincerely thank IISERM for financial support. N.Arora thanks CSIR, India for Research Fellowship. S.Das thanks DBT/Wellcome Trust India Alliance for Project Assistant Fellowship awarded to S.Rakshit. A.Kumar is grateful to DST Inspire for funding.

The authors declare no competing financial interests.

Author Contributions

S.Rakshit has supervised the project. G.S.Singaraju, S.Das, A.Sagar and A.Kumar did the cloning, expression, and purification. N.Arora performed and analysed AFM experiments.

G.S.Singaraju and C.S.Srinivas recorded and analysed droplet condensation and cell-aggregation experiments. C.S.Srinivas carried out the curve fitting. G.S.Singaraju, C.S.Srinivas, N.Arora and S.Rakshit made the figures. S.Rakshit and C.S.Srinivas wrote the manuscript. G.S.Singaraju, C.S.Srinivas, N.Arora and S.Rakshit edited the manuscript.

C.S.Srinivas and G.S.Singaraju have contributed equally.

References

- AMBADIPUDI, S., BIERNAT, J., RIEDEL, D., MANDELKOW, E. & ZWECKSTETTER, M. 2017. Liquid-liquid phase separation of the microtubule-binding repeats of the Alzheimer-related protein Tau. *Nature Communications*, 8, 275.
- BANJADE, S. & ROSEN, M. K. 2014. Phase transitions of multivalent proteins can promote clustering of membrane receptors. *Elife*, 3.
- BELL, G. I. 1978. Models for the specific adhesion of cells to cells. *Science*, 200, 618-27.
- BENZEKRY, S., LAMONT, C., BEHESHTI, A., TRACZ, A., EBOS, J. M., HLATKY, L. & HAHNFELDT, P. 2014. Classical mathematical models for description and prediction of experimental tumor growth. *PLoS Comput Biol*, 10, e1003800.
- BEUTEL, O., MARASPINI, R., POMBO-GARCIA, K., MARTIN-LEMAITRE, C. & HONIGMANN, A. 2019. Phase Separation of Zonula Occludens Proteins Drives Formation of Tight Junctions. *Cell*, 179, 923-936 e11.
- BUCHAN, J. R. & PARKER, R. 2009. Eukaryotic stress granules: the ins and outs of translation. *Mol Cell*, 36, 932-41.
- BUSTAMANTE, C., MARKO, J. F., SIGGIA, E. D. & SMITH, S. 1994. Entropic elasticity of lambda-phage DNA. *Science*, 265, 1599-600.
- CHOUDHARY, D., NARUI, Y., NEEL, B. L., WIMALASENA, L. N., KLANSECK, C. F., DE-LA-TORRE, P., CHEN, C., ARAYA-SECCHI, R., TAMILSELVAN, E. & SOTOMAYOR, M. 2020. Structural determinants of protocadherin-15 mechanics and function in hearing and balance perception. *Proc Natl Acad Sci U S A*, 117, 24837-24848.
- DELARUE, M., BRITTINGHAM, G. P., PFEFFER, S., SUROVTSEV, I. V., PINGLAY, S., KENNEDY, K. J., SCHAFFER, M., GUTIERREZ, J. I., SANG, D., POTEREWICZ, G., CHUNG, J. K., PLITZKO, J. M., GROVES, J. T., JACOBS-WAGNER, C., ENGEL, B. D. & HOLT, L. J. 2018. mTORC1 Controls Phase Separation and the Biophysical Properties of the Cytoplasm by Tuning Crowding. *Cell*, 174, 338-349 e20.
- DI PALMA, F., HOLME, R. H., BRYDA, E. C., BELYANTSEVA, I. A., PELLEGRINO, R., KACHAR, B., STEEL, K. P. & NOBEN-TRAUTH, K. 2001. Mutations in Cdh23, encoding a new type of cadherin, cause stereocilia disorganization in waltzer, the mouse model for Usher syndrome type 1D. *Nat Genet*, 27, 103-7.
- DIGNON, G. L., BEST, R. B. & MITTAL, J. 2020. Biomolecular Phase Separation: From Molecular Driving Forces to Macroscopic Properties. *Annu Rev Phys Chem*, 71, 53-75.

- DUSTER, R., KALTHEUNER, I. H., SCHMITZ, M. & GEYER, M. 2021. 1,6-Hexanediol, commonly used to dissolve liquid-liquid phase separated condensates, directly impairs kinase and phosphatase activities. *J Biol Chem*, 296, 100260.
- ELBAUM-GARFINKLE, S. 2019. Matter over mind: Liquid phase separation and neurodegeneration. *J Biol Chem*, 294, 7160-7168.
- EVANS, E. & RITCHIE, K. 1997. Dynamic strength of molecular adhesion bonds. *Biophys J*, 72, 1541-55.
- GALL, J. G. 2003. The centennial of the Cajal body. *Nat Rev Mol Cell Biol*, 4, 975-80.
- HARRISON, O. J., JIN, X., HONG, S., BAHNA, F., AHLSEN, G., BRASCH, J., WU, Y., VENDOME, J., FELSOVALYI, K., HAMPTON, C. M., TROYANOVSKY, R. B., BEN-SHAUL, A., FRANK, J., TROYANOVSKY, S. M., SHAPIRO, L. & HONIG, B. 2011. The extracellular architecture of adherens junctions revealed by crystal structures of type I cadherins. *Structure*, 19, 244-56.
- HAZRA, J. P., SAGAR, A., ARORA, N., DEB, D., KAUR, S. & RAKSHIT, S. 2019. Broken force dispersal network in tip-links by the mutations at the Ca(2+)-binding residues induces hearing-loss. *Biochem J*, 476, 2411-2425.
- HE, Y., LI, J. & ZHANG, M. 2019. Myosin VII, USH1C, and ANKS4B or USH1G Together Form Condensed Molecular Assembly via Liquid-Liquid Phase Separation. *Cell Rep*, 29, 974-986 e4.
- HIRANO, S. 2012. Western blot analysis. *Methods Mol Biol*, 926, 87-97.
- ITOH, Y., IIDA, S., TAMURA, S., NAGASHIMA, R., SHIRAKI, K., GOTO, T., HIBINO, K., IDE, S. & MAESHIMA, K. 2021. 1,6-hexanediol rapidly immobilizes and condenses chromatin in living human cells. *Life Sci Alliance*, 4.
- JAIGANESH, A., DE-LA-TORRE, P., PATEL, A. A., TERMINE, D. J., VELEZ-CORTES, F., CHEN, C. & SOTOMAYOR, M. 2018. Zooming in on Cadherin-23: Structural Diversity and Potential Mechanisms of Inherited Deafness. *Structure*, 26, 1210-1225 e4.
- KACHAR, B., PARAKKAL, M., KURC, M., ZHAO, Y. & GILLESPIE, P. G. 2000. High-resolution structure of hair-cell tip links. *Proc Natl Acad Sci U S A*, 97, 13336-41.
- KAUR, T., ALSHAREEDAH, I., WANG, W., NGO, J., MOOSA, M. M. & BANERJEE, P. R. 2019. Molecular Crowding Tunes Material States of Ribonucleoprotein Condensates. *Biomolecules*, 9.
- KLUS, P., BOLOGNESI, B., AGOSTINI, F., MARCHESE, D., ZANZONI, A. & TARTAGLIA, G. G. 2014. The cleverSuite approach for protein characterization: predictions of structural properties, solubility, chaperone requirements and RNA-binding abilities. *Bioinformatics*, 30, 1601-8.
- KUMAR, A., RIZVI, M. S., ATHILINGAM, T., PARIHAR, S. S. & SINHA, P. 2020. Heterophilic cell-cell adhesion of atypical cadherins Fat and Dachshous regulate epithelial cell size dynamics during *Drosophila thorax* morphogenesis. *Mol Biol Cell*, 31, 546-560.
- LATONEN, L. 2019. Phase-to-Phase With Nucleoli - Stress Responses, Protein Aggregation and Novel Roles of RNA. *Front Cell Neurosci*, 13, 151.
- LI, Q., CHENG, Z., ZHOU, L., DARMANIS, S., NEFF, N. F., OKAMOTO, J., GULATI, G., BENNETT, M. L., SUN, L. O., CLARKE, L. E., MARSCHALLINGER, J., YU, G., QUAKE, S. R., WYSS-CORAY, T. & BARRES, B. A. 2019. Developmental Heterogeneity of Microglia and Brain Myeloid Cells Revealed by Deep Single-Cell RNA Sequencing. *Neuron*, 101, 207-223 e10.
- MAHEN, R. & VENKITARAMAN, A. R. 2012. Pattern formation in centrosome assembly. *Curr Opin Cell Biol*, 24, 14-23.
- MCNEIL, E., CAPALDO, C. T. & MACARA, I. G. 2006. Zonula occludens-1 function in the assembly of tight junctions in Madin-Darby canine kidney epithelial cells. *Mol Biol Cell*, 17, 1922-32.

- MITCHELL, S. F., JAIN, S., SHE, M. & PARKER, R. 2013. Global analysis of yeast mRNPs. *Nat Struct Mol Biol*, 20, 127-33.
- POCZOBUTT, J. M., DE, S., YADAV, V. K., NGUYEN, T. T., LI, H., SIPPEL, T. R., WEISER-EVANS, M. C. & NEMENOFF, R. A. 2016. Expression Profiling of Macrophages Reveals Multiple Populations with Distinct Biological Roles in an Immunocompetent Orthotopic Model of Lung Cancer. *J Immunol*, 196, 2847-59.
- PONTANI, L. L., JORJADZE, I. & BRUJIC, J. 2016. Cis and Trans Cooperativity of E-Cadherin Mediates Adhesion in Biomimetic Lipid Droplets. *Biophys J*, 110, 391-399.
- SANNIGRAHI, M. K., SRINIVAS, C. S., DEOKATE, N. & RAKSHIT, S. 2019. The strong propensity of Cadherin-23 for aggregation inhibits cell migration. *Mol Oncol*, 13, 1092-1109.
- SINGARAJU, G. S., SAGAR, A., KUMAR, A., SAMUEL, J. S., HAZRA, J. P., SANNIGRAHI, M. K., YENNAMALLI, R. M., ASHISH, F. & RAKSHIT, S. 2019. Structural basis of the strong cell-cell junction formed by cadherin-23. *FEBS J*.
- SOTOMAYOR, M., WEIHOFEN, W. A., GAUDET, R. & COREY, D. P. 2010. Structural determinants of cadherin-23 function in hearing and deafness. *Neuron*, 66, 85-100.
- SOTOMAYOR, M., WEIHOFEN, W. A., GAUDET, R. & COREY, D. P. 2012. Structure of a force-conveying cadherin bond essential for inner-ear mechanotransduction. *Nature*, 492, 128-32.
- SRINIVASAN, S., HAZRA, J. P., SINGARAJU, G. S., DEB, D. & RAKSHIT, S. 2017. ESCORTing proteins directly from whole cell-lysate for single-molecule studies. *Anal Biochem*, 535, 35-42.
- THOMPSON, C. J., SU, Z., VU, V. H., WU, Y., LECKBAND, D. E. & SCHWARTZ, D. K. 2020. Cadherin clusters stabilized by a combination of specific and non-specific cis-interactions. *Elife*, 9.
- THOMPSON, C. J., VU, V. H., LECKBAND, D. E. & SCHWARTZ, D. K. 2019. Cadherin Extracellular Domain Clustering in the Absence of Trans-Interactions. *J Phys Chem Lett*, 10, 4528-4534.
- WANG, Z., ZHANG, G. & ZHANG, H. 2019. Protocol for analyzing protein liquid-liquid phase separation. *Biophysics Reports*, 5, 1-9.
- WEST, J. & NEWTON, P. K. 2019. Cellular interactions constrain tumor growth. *Proc Natl Acad Sci U S A*, 116, 1918-1923.
- WU, Y., JIN, X., HARRISON, O., SHAPIRO, L., HONIG, B. H. & BEN-SHAUL, A. 2010. Cooperativity between trans and cis interactions in cadherin-mediated junction formation. *Proc Natl Acad Sci U S A*, 107, 17592-7.
- ZHANG, Y., CHEN, K., SLOAN, S. A., BENNETT, M. L., SCHOLZE, A. R., O'KEEFFE, S., PHATNANI, H. P., GUARNIERI, P., CANEDA, C., RUDERISCH, N., DENG, S., LIDDELOW, S. A., ZHANG, C., DANEMAN, R., MANIATIS, T., BARRES, B. A. & WU, J. Q. 2014. An RNA-sequencing transcriptome and splicing database of glia, neurons, and vascular cells of the cerebral cortex. *J Neurosci*, 34, 11929-47.
- ZHANG, Y., SLOAN, S. A., CLARKE, L. E., CANEDA, C., PLAZA, C. A., BLUMENTHAL, P. D., VOGEL, H., STEINBERG, G. K., EDWARDS, M. S., LI, G., DUNCAN, J. A., 3RD, CHESHER, S. H., SHUER, L. M., CHANG, E. F., GRANT, G. A., GEPHART, M. G. & BARRES, B. A. 2016. Purification and Characterization of Progenitor and Mature Human Astrocytes Reveals Transcriptional and Functional Differences with Mouse. *Neuron*, 89, 37-53.

Abbreviations

AFM Atomic Force Microscope
Cdh23 Cadherin-23
CDF Cumulative Distribution Function
CD Cytosolic domain
DAPI 4,6-diamidino-2-phenylindole
EC Extracellular
EC1-10 Extracellular 1-10 domains
EC1-27 Extracellular 1-27 domains
eGFP Enhanced Green fluorescent protein
ESCORT Enzymatic Sortase-assisted Covalent Orientation-specific Restaint Tethering
1,6-HD 1,6-Hexanediol
LLPS Liquid- Liquid Phase Separation
Pcdh15 Protocadherin-15
qRT-PCR Quantitative Real-time polymerase chain reaction
SMFS Single-molecule force spectroscopy
TM Transmembrane

Figures and Table

Figure 1

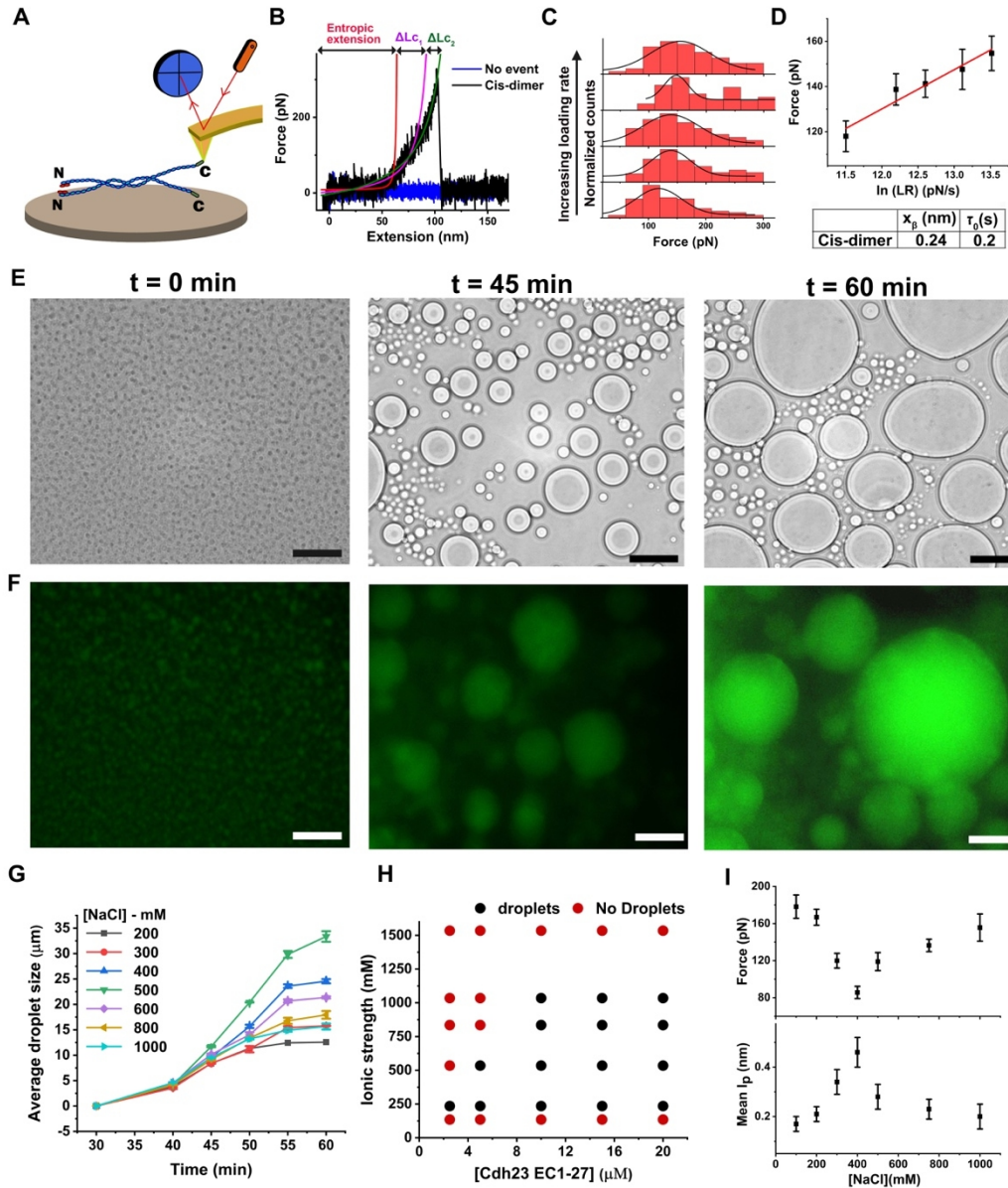


Figure 1. Cis-clustering drives LLPS of Cadherin-23. (A) Schematic representation of the SMFS experiment performed using AFM. The blue beads represent the individual EC domains of Cdh23. Red beads at the N-terminus of Cdh23 represent Pcdh15 EC1-2. (B) Representative force-extension trace (black) of cis-dimer rupturing, depicting an entropic extension followed by two unzipping and final unbinding of cis-dimer. Red, magenta, and green solid lines show the WLC fit to each extension. The

blue trace represents a typical no-interaction event. **(C)** Histograms of the cis-unbinding forces with increasing pulling velocities (1000, 2000, 3000, 5000, 7500 nm.s⁻¹). Solid black lines are the corresponding Gaussian fits. Peak maxima from the histogram are the most probable unbinding forces. **(D)** The linear increase of most probable unbinding forces (black squares) with increasing loading rates (in the natural log) together with the Bell-Evans model fit (solid line). Error bars are the standard error from the Gaussian fits from figure C. Kinetic parameters, distance to transition state (x_{β}) and intrinsic lifetime (τ_0), obtained from the Bell-Evans fit are given in the table. **(E)** Representative bright-field images, and **(F)** fluorescence images of liquid droplet-like condensates of Cdh23 EC1-27 at three different time intervals (i) 0 min, (ii) 45 min, and (iii) 60 min. Buffer composition is 20 mM HEPES, 500 mM NaCl and 6 mM CaCl₂. Scale bar: 50 μ m. **(G)** Growth kinetics of liquid droplets (μ m) at a varying concentration of NaCl. Error bars represent the standard error of the mean (SEM) with N=30 droplets. **(H)** Phase diagram of liquid droplets of Cdh23 EC1-27 relating protein concentration and ionic strength of the buffer with droplet formation. **(I)** Overlay plots of the variations in the most probable unbinding force (upper panel) and the mean persistence length (lower panel) of the cis-dimers with the ionic strength of the buffer. Error bars in force are from the standard error of Gaussian fitting, whereas the standard error of the mean for the persistence length (N~30).

Figure 2

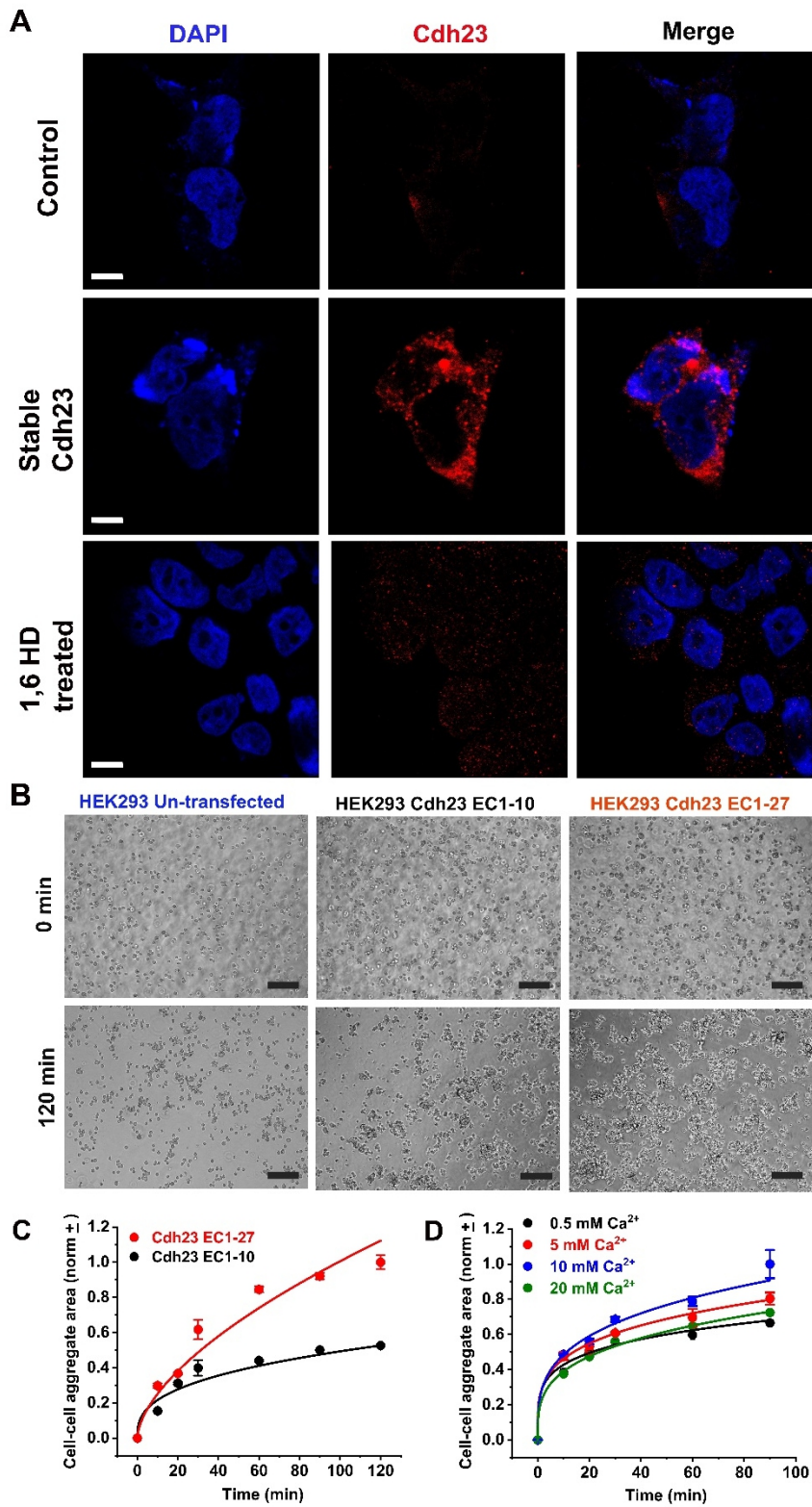


Figure 2. LLPS of Cdh23 facilitates cell-cell attachment. (A) The immunofluorescence images of the puncta (red) of Cdh23 on HEK293 cells exogenously expressing Cdh23 (Middle row). No puncta were noticed in control (top row). Bottom row: Disruption of puncta after 1,6-Hexanediol (1,6-HD) treatment to HEK293 cells exogenously expressing Cdh23. DAPI is to stain the nucleus (blue). Scale bar: 10 μm . (B) Time-stamp bright-field images of cell-cell aggregations of HEK293 cells untransfected (1st column), transiently transfected with Cdh23 EC1-10 (2nd column), and Cdh23 EC1-27 (3rd column). Scale bar: 50 μm . (C) The time-dependent growth of the cell-cell aggregation area (normalized) of HEK293 cells exogenously expressing Cdh23 EC1-27 (red) and Cdh23 EC1-10 (black), along with the Von Bertalanffy model fit (solid lines). The error bars represent the standard error of the mean (SEM) with N=15 aggregates. (D) The time-dependent growth of the cell-cell aggregation area (normalized) of HEK293 cells exogenously expressing Cdh23 EC1-27 at varying calcium concentrations. The error bars represent the standard error of the mean (SEM) for N=15 aggregates. The solid lines represent the fitting of aggregation kinetics to the Von Bertalanffy model.

Figure 3

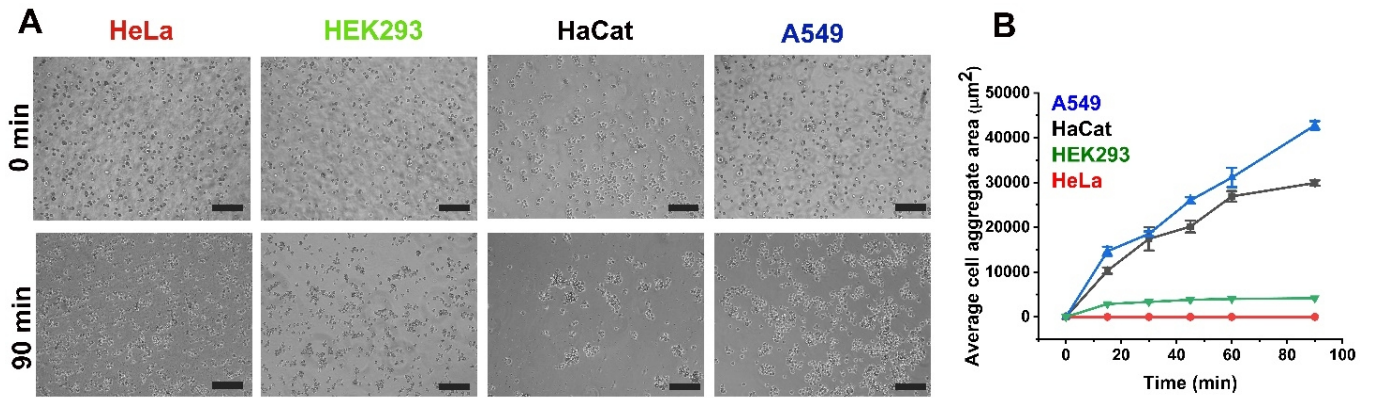


Figure 3. Dependence of cell-cell attachment rate on the intrinsic expression of Cdh23. (A) Time-stamp bright-field images of cell-aggregates of HeLa, HEK293, HaCat, and A549 cells differentially expressing endogenous Cdh23. Scale bar: 50 μm . (B) Growth of cell-cell aggregation area (in μm^2) with time for HeLa (red), HEK293 (green), HaCat (black) and A549 (blue) cell lines. Error bars represent the standard error of the mean (SEM) for N=15 aggregates.

Table1. CDF scores for different cadherins (ectodomains only) estimated by catGRANULEalgorithm.

Cadherins	CDF score
<i>Cdh23</i>	1.259
<i>Pcdh1</i>	1.002
<i>Dcsh1</i>	1.350
<i>FAT1</i>	1.432
<i>FAT2</i>	1.326
<i>FAT3</i>	1.538
<i>FAT4</i>	1.642

CDF score represents the propensity for LLPS

Supplementary Files

This is a list of supplementary files associated with this preprint. Click to download.

- [FusionEventFIVideo1A.mp4](#)
- [supplementaryfilenaturecommunications.pdf](#)
- [FusionEventBFVideo1B.mp4](#)
- [supplementaryfilenaturecommunications.pdf](#)